Discovery of polyphenolic natural products as SARS-CoV-2 Mpro inhibitors for COVID-19

Nadine Krüger,[1,≠] Thales Kronenberger,[2,3,≠] Hang Xie,[4,≠] Cheila Rocha,[1,5] Stefan Pöhlmann,[1,5] Haixia Su,[6] Yechun Xu,[4,6,*] Stefan A. Laufer,[2] and Thanigaimalai Pillaiyar[2,≠,*]

[1]Infection Biology Unit, German Primate Center, Leibniz Institute for Primate Research Göttingen, Kellnerweg 4, Göttingen 37077, Germany

[2]Institute of Pharmacy, Pharmaceutical/Medicinal Chemistry and Tübingen Center for Academic Drug Discovery, Eberhard Karls University Tübingen, Auf der Morgenstelle 8, 72076 Tübingen, Germany

[3]Cluster of Excellence iFIT (EXC 2180) "Image-Guided & Functionally Instructed Tumor Therapies", University of Tübingen, Tübingen 72076, Germany

[4]School of Chinese Materia Medica, Nanjing University of Chinese Medicine, Nanjing 210023, China

[5]Faculty of Biology and Psychology, Georg-August-University Göttingen, Göttingen, Germany

[6]CAS Key Laboratory of Receptor Research, and State Key Laboratory of Drug Research, Shanghai Institute of Materia Medica, Chinese Academy of Sciences, Shanghai 201203, China

[≠]These authors contributed equally

*Correspondence: Email: thanigaimalai.pillaiyar@uni-tuebingen.de; Tel.: +49-7071-2977458: E-mail: ycxu@simm.ac.cn; Tel.: 0086-21-50801267

 doi:10.20944/preprints202211.0516.v1

Abstract

The severe acute respiratory syndrome coronavirus 2 (SARS-CoV-2) has forced the development of direct-acting antiviral drugs due to the coronavirus disease 2019 (COVID-19) pandemic. The main protease of SARS-CoV-2 is a crucial enzyme that breaks down polyproteins synthesized from the viral RNA, making it a validated target for the development of SARS-CoV-2 therapeutics. New chemical phenotypes are frequently discovered in natural goods. In the current study, we used a fluorogenic assay to test a variety of natural products for their ability to inhibit SARS-CoV-2 M^{pro}. Several compounds were discovered to inhibit the M^{pro} at low micromolar concentrations. It was possible to crystallize robinetin together with SARS-CoV-2 M^{pro}, and the X-ray structure revealed covalent interaction with the protease's catalytic Cys145 site. Selected potent molecules also exhibited antiviral properties without cytotoxicity. Some of these powerful inhibitors might be utilized as lead compounds for COVID-19 research.

Keywords: Antivirals, coronavirus, COVID-19, covalent drugs, dynamic light scattering, inhibitors, main protease, natural products.

 doi:10.20944/preprints202211.0516.v1

1. Introduction

Human coronaviruses like the Middle East respiratory syndrome coronavirus (MERS-CoV), severe acute respiratory syndrome coronavirus 2 (SARS-CoV-2), and SARS-CoV-1 emerged since the turn of the twenty-first century and have caused three epidemics that pose serious risks to both public health and the economy [1]. In particular, the SARS-CoV-2-related ongoing pandemic coronavirus disease 2019 (COVID-19) has killed about 7 million people and infected approximately 635 million people worldwide. The numbers are still rising. Numerous common molecular characteristics between SARS-CoV-1 and other bat coronaviruses can be found in SARS-CoV-2, a coronavirus from the genus beta-coronavirus [2]. With co-morbid conditions, it is highly contagious and fatal for elderly patients [3,4]. A primary objective is the development of a potent antiviral drug, and various viral targets have been considered. As of right now, the three antiviral medications approved by the FDA for the treatment of COVID-19 infection are remdesivir and molnupiravir, both targeting the viral RNA-dependent RNA polymerase (RdRp), as well as nirmatrelvir, targeting the SARS-CoV-2 M^{pro}. Additionally, a variety of peptidomimetic compounds that successfully inhibit specific SARS-CoV-2 proteases have been identified [5–9], and many medications have been investigated for potential repurposing as COVID-19 treatments [10].

Members of the family Coronaviridae, including seven human coronaviruses, harbour a positive-sense single-stranded RNA genome [11]. Host ribosomes translate the genome of these enveloped viruses into the two polyproteins PP1a and PP1b [1,12].

Preprints (www.preprints.org) | NOT PEER-REVIEWED | Posted: 28 November 2022 doi:10.20944/preprints202211.0516.v1

The main protease, also known as chymotrypsin-like protease or 3C-like protease ($3CL^{pro}$), and a papain-like protease (PL^{pro}), cleave the polyproteins to produce mature non-structural functional proteins, such as RdRp and helicase, which are necessary for the completion of the viral replication cycle [13].

The majority of the cleavage of viral proteins by M^{pro} occurs at least 11 times, with substrate specificity exhibited by the efficient cleavage of peptides such as (Leu, Phe, Met, Val)-Gln↓ (Ser, Ala, Gly) sequences (the cleavage site is indicated by ↓). It has also been well established that the substrate-binding sites exhibit an incredibly high degree of conservation, particularly for the critical S1/S2 subsite [14–16]. Because of its critical role in processing polyproteins, high degree of conservation, absence of a human analog protease, and involvement in polyprotein processing, M^{pro} is an attractive target for the development of broad-spectrum antiviral drugs. Numerous M^{pro} inhibitors consist of substrate-derived peptides and small molecules with a covalent or noncovalent mechanism of action [11,12,17]. As M^{pro} is one of the most well-characterized therapeutic targets among CoV [5,7,18], finding new M^{pro} inhibitors with various chemical structures is essential to accelerating drug development against highly pathogenic CoVs.

Natural products are an important source of new chemical phenotypes, and the natural phytochemicals that exhibit anti-CoV activity have been extensively summarized [19,20]. Xu, Y. *et al.* recently reported several natural polyphenolic compounds as covalent inhibitors of SARS-CoV-2 M^{pro} and identified pyrogallol as a novel warhead moiety [21,22]. In the present study, we collected several electrophilic

Preprints (www.preprints.org) | NOT PEER-REVIEWED | Posted: 28 November 2022 doi:10.20944/preprints202211.0516.v1

natural products and polyphenolic compounds and investigated them for their M^{pro} inhibitory activities. Additionally, the co-crystal structure of SARS-CoV-2 M^{pro} in complex with robinetin was determined, which confirmed the covalent bond formation. Selected active compounds were further tested in Calu-3 cells for antiviral activities.

2. Results and discussion

2.1. The M^{pro} inhibition assay: The assay was carried out using a newly developed fluorogenic substrate (Dacyl- KTSAVLQSGFRKME-Edans), as previously described [22]. A fluorescence resonance energy transfer (FRET) protease assay was utilized to measure the inhibitory activity of the investigated compounds against the SARS-CoV-2 M^{pro}. Each compound was tested at a concentration of 10 μM, and for the compound that showed >30% inhibition, the half-maximum concentration (IC_{50}) was measured (Table 1).

Table 1. Inhibition of SARS-CoV-2 M^{pro} by natural and inspired compounds

Chemical structure	SARS-CoV-2 M^{pro}	
	% Inhibition at 10 μM	IC_{50} (μM)
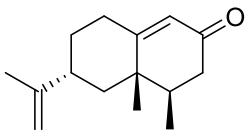 **(+)-Nootkaton**	32.04	>10
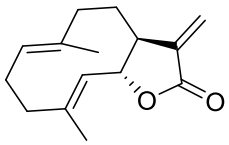	27.96	>10

Preprints (www.preprints.org) | NOT PEER-REVIEWED | Posted: 28 November 2022 doi:10.20944/preprints202211.0516.v1

Costunolide 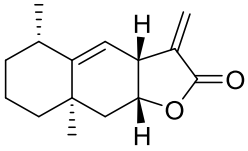	27.55	>10
Alantolacton 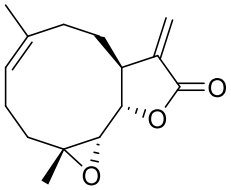	20.06	>10
(-)-Parthenolide 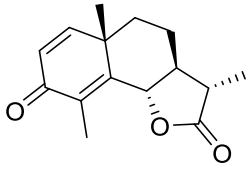	24.13	>10
(–)-*α*-Santonin 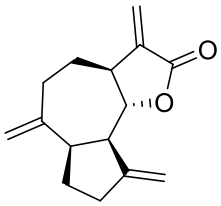	13.39	>10
Dehydrocostus lactone 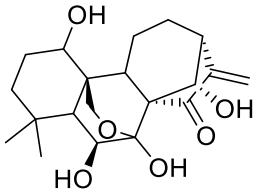	81.87	**4.67**
Oridonin 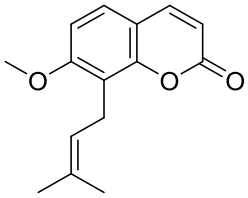	4.98	>10
Osthole 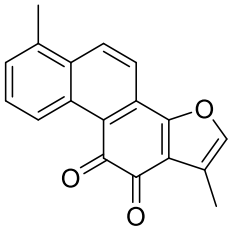	7.03	>10
Tanshinone I		

Preprints (www.preprints.org) | NOT PEER-REVIEWED | Posted: 28 November 2022 doi:10.20944/preprints202211.0516.v1

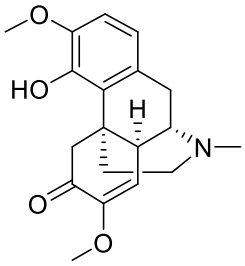 **Sinomenine**	4.80	>10
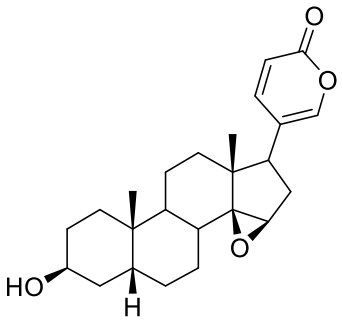 **Resibufogenin**	6.32	>10
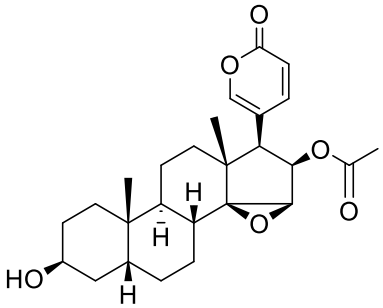 **Cinobufagin**	0.53	>10
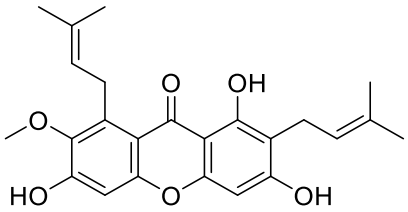 ***α*-Mangostin**	38.56	**25.12**
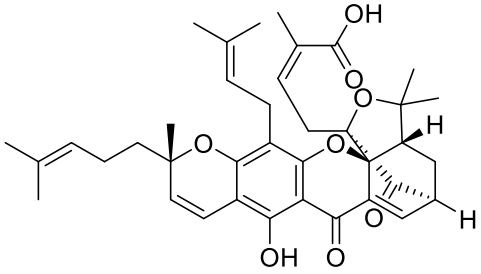 **Gambogic acid**	22.75	>10

Preprints (www.preprints.org) | NOT PEER-REVIEWED | Posted: 28 November 2022 doi:10.20944/preprints202211.0516.v1

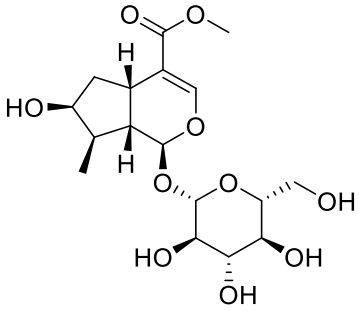 **Loganin**	29.43	>10
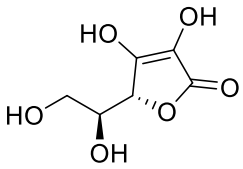 **L-Ascorbic acid**	22.25	>10
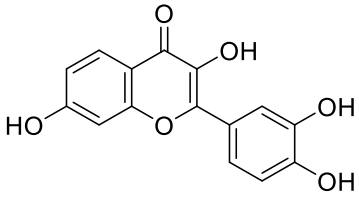 **Fisetin**	-11.21	>10
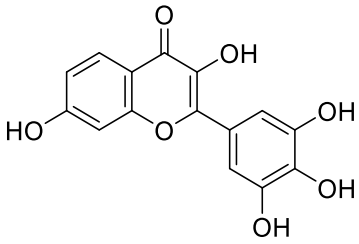 **Robinetin**	86.13	**0.96**
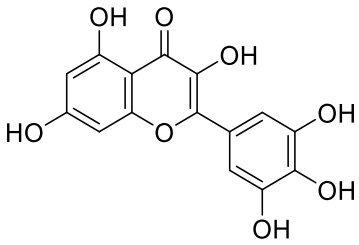 **Myricetin**	104.00	**0.645**
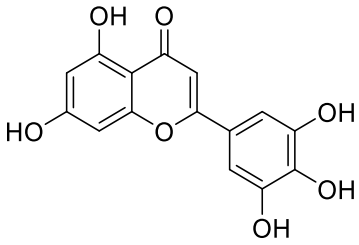 **Tricetin**	72.28	**7.84**

Preprints (www.preprints.org) | NOT PEER-REVIEWED | Posted: 28 November 2022 doi:10.20944/preprints202211.0516.v1

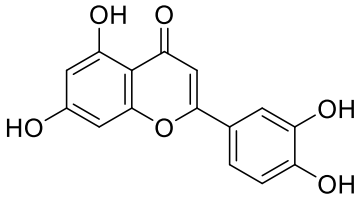 **Luteoline**	9.65	>10
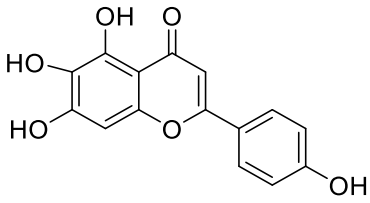 **Scutellarein**	76.07	**6.07**
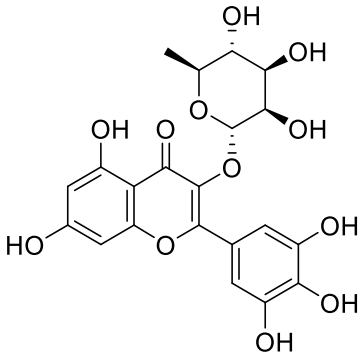 **Myricitrin**	11.67	>10
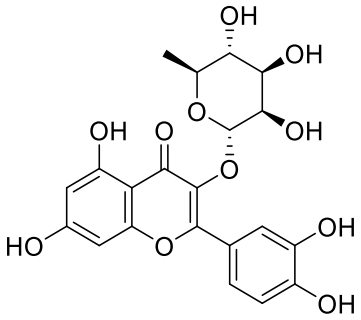 **Quercitrin**	2.42	>10
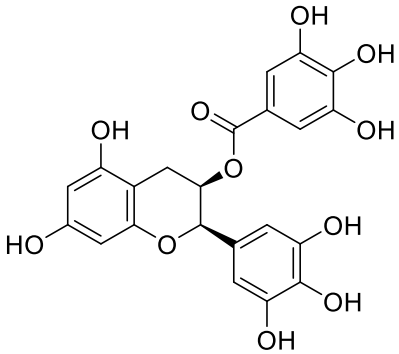 **L-Epigallocatechin gallate**	105.40	**0.228**

Preprints (www.preprints.org) | NOT PEER-REVIEWED | Posted: 28 November 2022 doi:10.20944/preprints202211.0516.v1

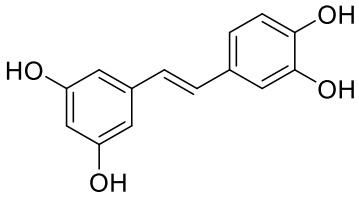 **Piceatannol**	76.90	**2.031**
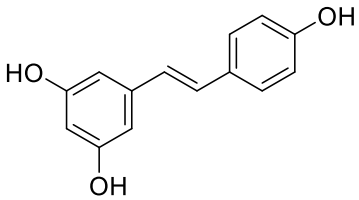 **Resveratrol**	5.96	>10
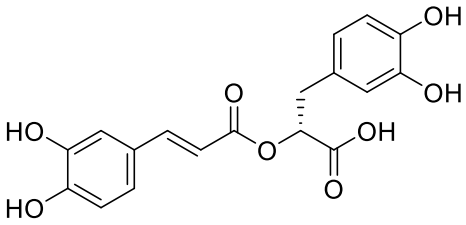 **Rosmarinic acid**	50.56	**6.84**
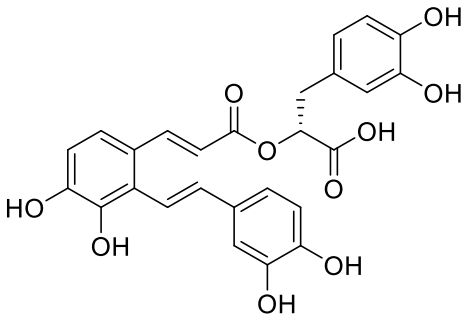 **Salvianolic acid A**	50.84	**28.38**
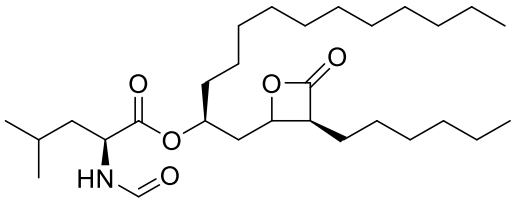 **Orlistat**	20.99	>10
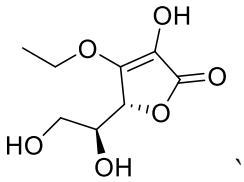 **3-O-Ethyl-L-ascorbic acid**	24.94	>10

Preprints (www.preprints.org) | NOT PEER-REVIEWED | Posted: 28 November 2022 doi:10.20944/preprints202211.0516.v1

The bicyclic conjugated sesquiterpene ketone (+)-nootkatone, which resembles a grapefruit, is widely utilized in the food, fragrance, cosmetics, and pharmaceutical industries [23,24]. The active ingredient in *Cyperus rotundus*, a well-known oriental traditional medicine, is (+)-nootkatone, which has antiplatelet properties. Additionally, there was proof of potential effectiveness against *Staphylococcus aureus* biofilms. (+)-Nootkatone was selected as a potential candidate as it contains the Michael acceptor in the ring system that might be reactive towards the Cys145 of M^{pro}, but it demonstrated only a moderate inhibition (32.04%).

Oridonin is a bioactive ent-kaurane diterpenoid natural product isolated from *Rabdosia rubescens* that has been widely used in traditional Chinese medicine [25,26]. As reported previously, oridonin possesses anti-tumor, anti-bacterial, and anti-inflammatory effects. Oridonin has been demonstrated to inhibit NF-B or MAPK activation to reduce the release of proinflammatory cytokines like tumor necrosis factor (TNF) and interleukin (IL)-6 [27–29] that play a crucial role in the process known as cytokine storm, a dicey signal that may result in the death of patients with severe COVID-19. Oridonin's molecular targets have been identified as the AKT1 and AKT2 inflammasomes, as well as the NLRP3 inflammasome [30]. A recent study revealed that oridonin covalently modifies the NLRP3 inflammasome, targeting the cysteine 279 of NLRP3 [31].

Oridonin has been identified as an inhibitor of M^{pro} with an IC_{50} value of 4.67 μM, which confirmed the previous study with its M^{pro} inhibitory activity (IC_{50} 2.16 μM [32]), and we learned from the literature that Oridonin covalently modifies the M^{pro}

Preprints (www.preprints.org) | NOT PEER-REVIEWED | Posted: 28 November 2022 doi:10.20944/preprints202211.0516.v1

targeting Cys145. M^{pro} crystal structure in complex with oridonin (PDB ID: 7VIC [32], Resolution: 2.10 Å, Figure 1) not only confirms the Cys145-covalent bond previously shown by mass spectrometry and kinetic studies but also shows one unique covalent binding mechanism not relying on peptidomimmetics. Oridonin is stabilized by the classical hydrogen bond interaction with Glu166's backbone and its hydroxyl group, with the support of hydrophobic interactions with the side-chains of Met49 and Met165, as well as His41 and His163, to some extent.

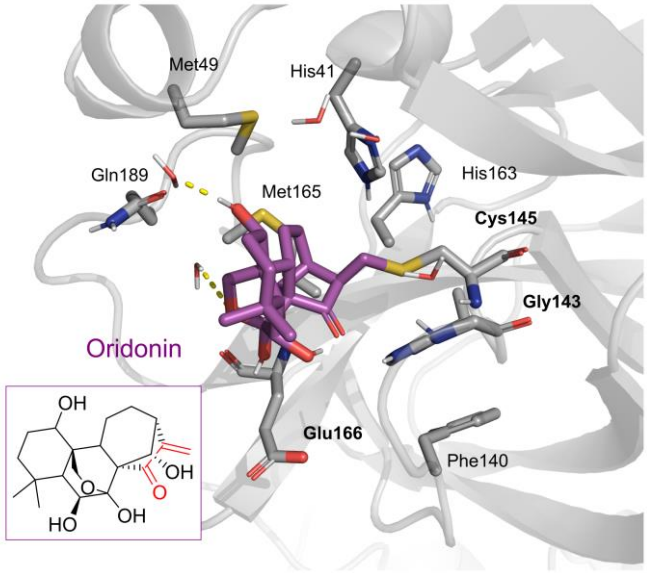

Figure 1. Oridonin binding mode in the M^{pro} binding site, determined by crystallography (PDB ID 7VIC).

The xanthone alpha-mangostin**,** which has been discovered in *G. mangostana*, exhibits a variety of biological effects. Fatty acid synthase and HIV-1 protease are both inhibited by it (IC_{50} values of 5.54 and 5.12 μM, respectively). Alpha-mangostin is effective against methicillin-sensitive and *S. aureus*-resistant strains. It reduces the synthesis of prostaglandin E2 (PGE2, Cay-14010) and nitric oxide (IC_{50}'s: 12.4 and

Preprints (www.preprints.org) | NOT PEER-REVIEWED | Posted: 28 November 2022 doi:10.20944/preprints202211.0516.v1

11.1 μM, respectively). Alpha-mangostin exhibited weak M^{pro} inhibition with an IC_{50} value of 25.12 μM.

Robinetin, also known as 5-deoxymyricetin, is a bioactive natural flavonoid. The compound is known for its anti-mutagenesis [33], antitumorgenicity [34], and atheroprotective effect [35]. Recent computational work suggests that it could be a potential candidate as a M^{pro} of SAR-CoV-2 inhibitor [36]. In our testing conditions, this compound significantly inhibited the M^{pro}, with an IC_{50} value of 0.96 μM. The potency of robinetin is almost similar to that of myricetin (IC_{50} 0.649 μM) whose M^{pro} inhibitory activity confirmed once again in the present study. In contrast, Fisetin, which bears catechol in ring C, showed only 11% M^{pro} inhibition, suggesting the presence of pyrogallol is important for the M^{pro} inhibition.

To precisely illustrate the binding mode of the inhibitor, a crystal structure of the SARS-CoV-2 M^{pro} in complex with robinetin was determined at 2.28 Å resolution (PDB ID:8HI9, Figure 2). Robinetin bound into the substrate-binding site at the surface of the protease and mainly occupies S1 and S2 subsites, similar to the binding mode of myricetin with the M^{pro} [21]. At S1 subsite, the pyrogallol ring establishes a covalent bond with the catalytic residue Cys145. In addition to this covalent binding interaction, the pyrogallol group's hydroxyl displays hydrogen bonds with the backbone of Gly143/Cys145/Thr26 (part of the oxyanion hole). At S2 subsite, two hydroxyl groups of the chromone moiety form hydrogen bonds with the side chain carboxyl group of Glu166 and Tyr54 through a water molecule, respectively. Additionally, the carbonyl group of the chromone moiety establishes hydrogen bonds

Preprints (www.preprints.org) | NOT PEER-REVIEWED | Posted: 28 November 2022 doi:10.20944/preprints202211.0516.v1

with the main chain of Glu166 and Gln189 through a water molecule. Moreover, robinetin is also stabilized by hydrophobic interactions with the side chains of Met49/Met165/His41/Thr26. Overall, the crystal structure revealed a covalent binding mode of robinetin to the catalytic site of the SARS-CoV-2 M^{pro} using the pyrogallol ring as a reaction warhead.

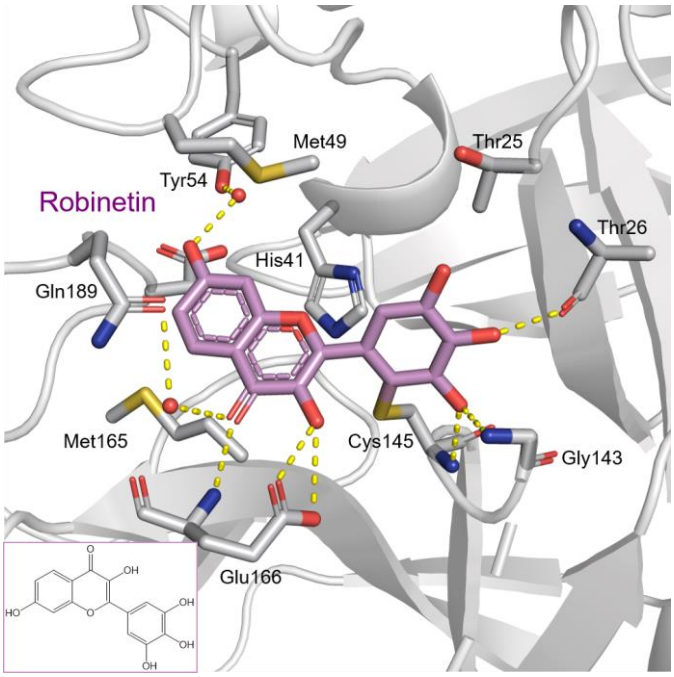

Figure 2. The covalent binding mode of robinetin in the M^{pro} ligand binding site revealed by X-ray crystal structure (PDB code: 8HI9)

Myricetin, a naturally occurring flavonol found in edible plants, has antimutagenic and anticarcinogenic properties. Myricetin inhibits M^{pro} with an IC_{50} value of 0.645 μM at a concentration of 10 μM. Recently, Xu, Y. *et al.* discovered that myricetin had M^{pro} inhibitory action [21]. The molecule's binding mode demonstrated that the pyrogallol group functioned as an electrophile to covalently alter the catalytic cysteine.

Preprints (www.preprints.org) | NOT PEER-REVIEWED | Posted: 28 November 2022 doi:10.20944/preprints202211.0516.v1

Tricetin activates the Nrf2/HO-1 signaling pathway, protecting against 6-OHDA-induced neurotoxicity in the Parkinson's disease model. It effectively inhibits the protein-protein interaction of Keap1-Nrf2 [37]. It had a weaker inhibitory effect on the M^{pro} than its 3-OH derivative, myricetin, with an IC_{50} value of 7.84 μM. It is conceivable that the 3-OH in myricetin or robinetin facilitates hydrogen bonding with the residues in the M^{pro} active site. Tricetin's putative binding mode (Figure 3) suggests a similar binding mode to its derivatives myricetin and robinetin, resulting in covalent interaction between the pyrogallol ring and Cys145. The oxygen in the pyrone ring forms an H-bond interaction with His41, and the catechol hydroxyls form H-bond interactions with Gln189 and Arg188, respectively.

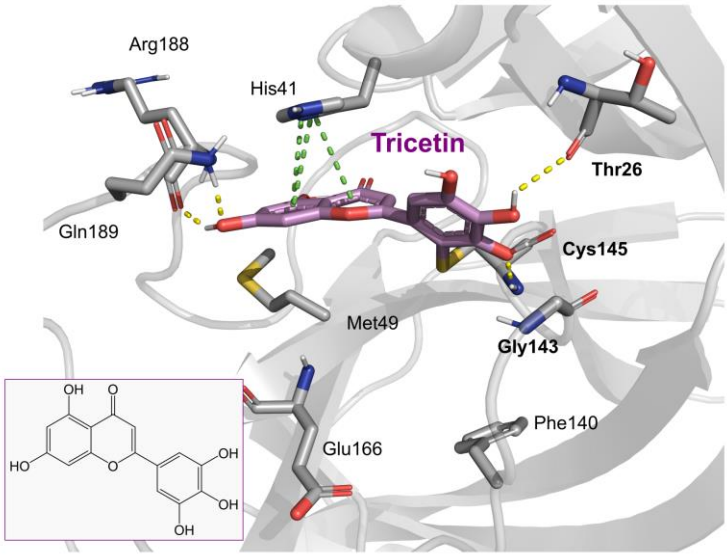

Figure 3. The putative tricetin binding mode in the M^{pro} binding site

Another flavonoid, luteoline, a potent Nrf2 inhibitor, was unable to inhibit the M^{pro} at the concentration of 10 μM. Interestingly, scutellarein, the main bioactive component extracted from *Erigeron breviscapus*, inhibited the M^{pro} with moderate potency and an

Preprints (www.preprints.org) | NOT PEER-REVIEWED | Posted: 28 November 2022 doi:10.20944/preprints202211.0516.v1

IC_{50} value of 6.07 μM, confirming previous findings [38,39]. Despite containing the pyrogallol unit in its core structure, the natural product myricitrin, the 3-O-L-rhamnopyranoside of myricetin, did not inhibit the M^{pro}. It suggested that the 3-O-L-rhamnopyranoside might have the necessary steric clashes to interact with the enzyme. Quercitrin was also unable to inhibit the M^{pro} enzyme.

Chinese herbal medicine contains the compound EGCG (CHM). The tea leaf, especially green tea, is a rich source of the polyphenol catechin EGCG [40]. Just a few of the viruses that EGCG has proven to be effective against include adenovirus, influenza, Zika, herpesvirus, and hepatitis virus [41]. Zuo *et al*. in particular showed that EGCG has an inhibitory effect on the NS3 serine protease of the hepatitis C virus (HCV) [42]. EGCG was found to inhibit SARS-CoV-2 M^{pro} in *in vitro* studies, with an IC_{50} value of 73 μM [43]. It was recently found to inhibit SARS-CoV-2 M^{pro} with IC_{50} values ranging from 0.874 to 4.24 μM [44,45]. In our investigation, EGCG was able to completely inhibit the SARS-CoV-2 M^{pro} activity (IC_{50} value of 0.228 μM). Interestingly, the host suffers significant damage from proinflammatory cytokines that are overproduced [46]. The need for drugs that can treat COVID-19 hyper-inflammation is therefore very high in the clinical and research communities. EGCG may be a promising therapy for COVID-19 in this regard to reverse hyperinflammation. Previous research has shown that EGCG can effectively block the JAK/STAT pathway, which controls the production and release of a number of cytokines and chemokines [47,48]. Additionally, EGCG has been shown to inhibit the canonical NF-κB pathway [49,50], which is crucial for controlling the expression of

Preprints (www.preprints.org) | NOT PEER-REVIEWED | Posted: 28 November 2022 doi:10.20944/preprints202211.0516.v1

proinflammatory cytokines such as IL-1, TNF-α, IL-8, and IL-6. Both COVID-19 and cytokine storm syndrome generate all of these cytokines. Due to its low toxicity and potent intestinal absorption, EGCG also has additional benefits [51]. EGCG proposed binding mode relies on the covalent binding to Cys145, similarly to robitenin. The benzenetriol moiety stablishing multiple hydrogen bond interactions with the backbone atoms of Gly143, Cys145 and side-chain of Ser144 in the S1 (Figure 4). The second benzenetriol moiety occupies the pocket between Glu166 and Phe140, stablishing hydrogen bond interactions with those parts. Lastly, the chromone moiety interacts with the Gln189 and is stabilized by stacking interactions with the His41.

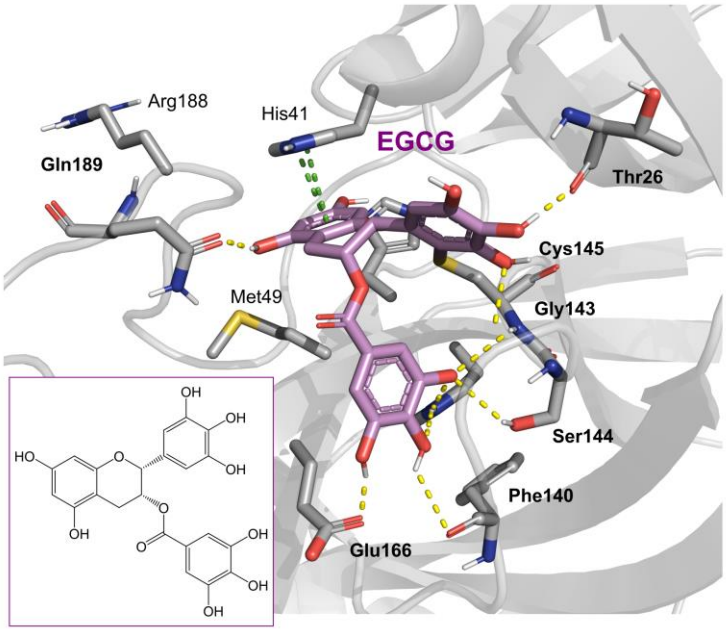

Figure 4. Potential binding mode of EGCG in the M^{pro} active site.

Figure 5 summarizes the structure-activity relationships of these polyphenolic compounds at the SARS-CoV-2 M^{pro}. In general, it was found that the trihydroxyl groups (pyrogallol) in either ring A or B were crucial for the M^{pro} inhibitory activity.

Preprints (www.preprints.org) | NOT PEER-REVIEWED | Posted: 28 November 2022 doi:10.20944/preprints202211.0516.v1

This outcome confirms the earlier discovery that pyrogallol is a novel covalent warhead group for the development of SARS-CoV-2 M^{pro} inhibitors [21]. Myricitrin did not, however, inhibit the M^{pro}, even though its core structure includes a pyrogallol unit. It suggested the 3-*O*-*α*-*L*-rhamnopyranoside might have steric clashes to interact with the enzyme. It was discovered that the molecule's catechol unit had no effect on M^{pro} activity (compare fisetin vs. robinetin; luteoline vs. tricetin). The M^{pro} inhibitory activity is favoured by the molecules' presence of a hydroxyl group at position 3 on ring B (compare tricetin vs myricetin). On the other hand, it was revealed that the presence of a 4-hydroxy group in ring C decreased inhibitory activity when compared to scutellarein and baicalein. In the current study, EGCG was discovered to be the most potent M^{pro} inhibitor.

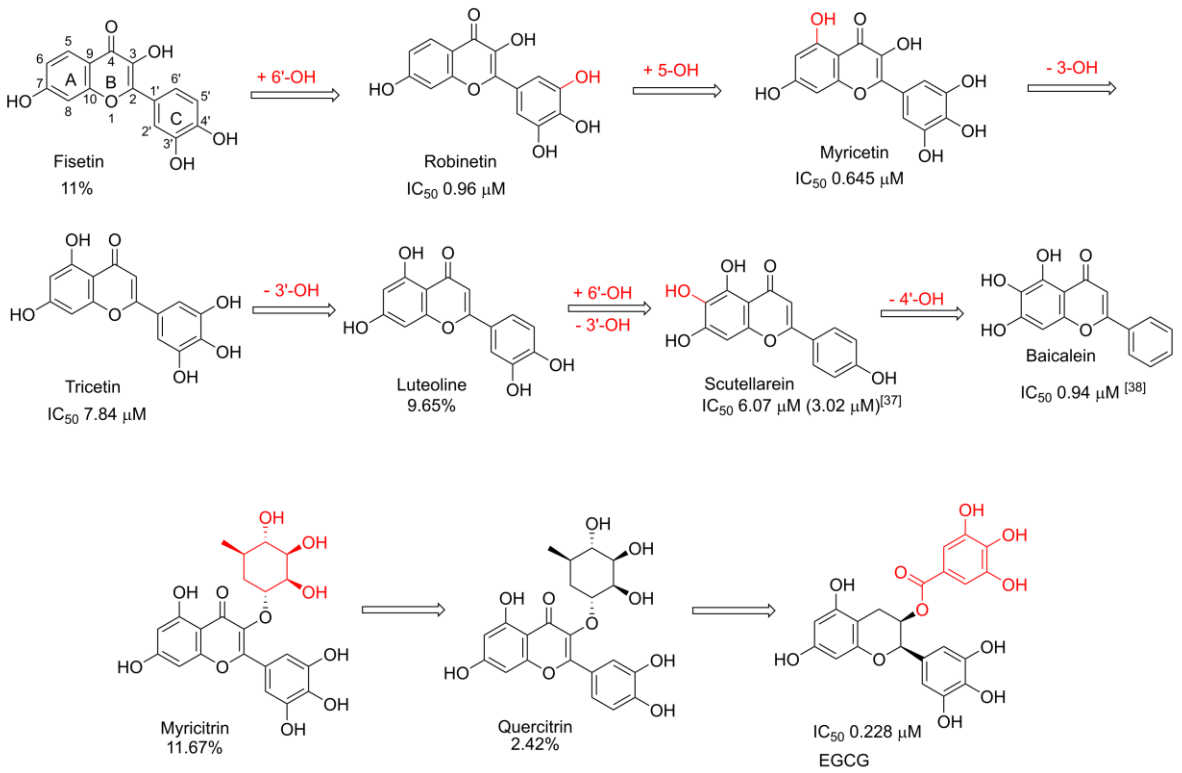

Figure 5. The structure activity relationships of polyphenolic compounds

Preprints (www.preprints.org) | NOT PEER-REVIEWED | Posted: 28 November 2022 doi:10.20944/preprints202211.0516.v1

Piceatannol is a bioactive stilbenoid of the catechol type that is present in both mycorrhizal and non-mycorrhizal roots of Norway spruces (*Picea abies*) [52]. Additionally, it is present in the seeds of the palm. It is a resveratrol metabolite. The protein kinase A subunit, pKC, and MLC are all reversibly inhibited by this cell-permeable substrate. Piceatannol inhibited LMP2A [53], a viral protein-tyrosine kinase thought to be involved in leukemia, non-lymphoma, Hodgkin's disease, and other illnesses connected to the Epstein-Barr virus. Piceatannol inhibits the M^{pro} with an IC_{50} value of 2.03 µM. However, its parent molecule, resveratrol, was unable to inhibit the enzyme. The molecular docking study suggests that the catechol unit in piceatannol is crucial for the inhibitory activity as one of the catechol rings interacts with the P1 pocket (Cys145, Figure 6) of M^{pro}, which is missing in the case of resveratrol. Meanwhile, the resorcinol ring stabilizes pi-pi interactions with His41 and further polar contacts with Gln189.

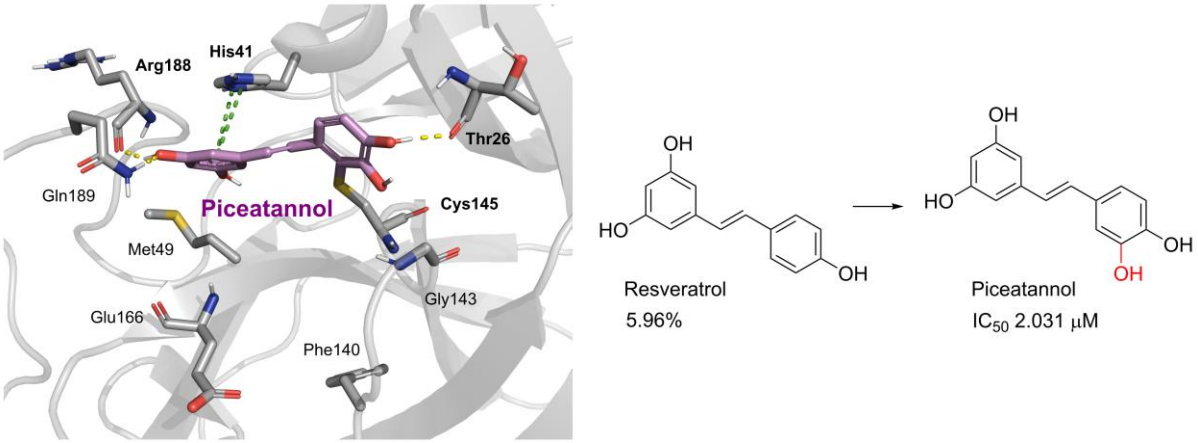

Figure 6. Docking study of Piceatannol in the M^{pro} binding site

Preprints (www.preprints.org) | NOT PEER-REVIEWED | Posted: 28 November 2022 doi:10.20944/preprints202211.0516.v1

Rosmarinic acid, a naturally occurring substance obtained from the plant rosemary (*Rosmarinus officinalis*) [54,55], is chemically the ester of caffeic acid with 3,4-dihydroxyphenyl)-lactic acid. This substance has been shown to have antiviral, antibacterial, and anti-inflammatory effects [56]. Because of this, it is utilized in a number of lemon balm remedies [57] as well as several ointments for sports injuries. The formation of orthoquinones by oxidation of the phenolic hydroxyl groups in rosmarinic acid is well recognized. These associate with peptides and subsequently render them inactive [58]. In our work, rosmarinic acid inhibited the M^{pro} with an IC_{50} value of 6.84 μM. We propose that it might covalently alter the M^{pro}: reactions between Cys145 and the Michael acceptor donnor, instead of orthoquinone generated by oxidizing the phenolic hydroxyl groups of rosmarinic acid, as originally proposed by other groups. Covalently bound rosmarinic acid frees the hydroxyl groups to interact with the His163 and the Glu166's backbone (Figure 7).

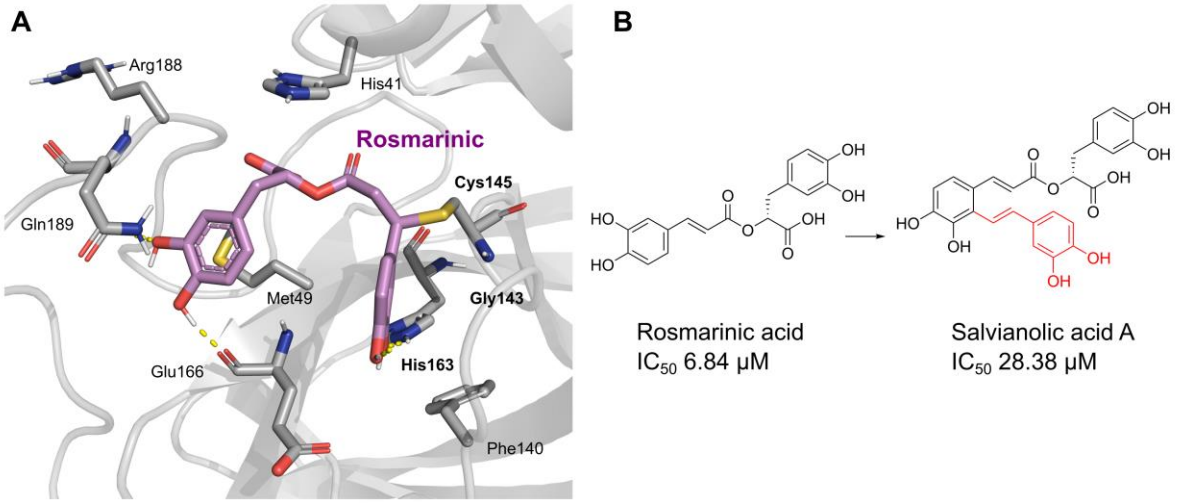

Figure 7. Rosmarinic potential binding mode within the M^{pro} catalytic binding site.

Preprints (www.preprints.org) | NOT PEER-REVIEWED | Posted: 28 November 2022 doi:10.20944/preprints202211.0516.v1

Salvianolic acid A, also known as Dan Phenolic Acid A, is a water-soluble chemical that is derived from Radix Salvia miltiorrhiza (Danshen). It has antioxidant and free radical-scavenging properties, and it also prevents protein-protein interactions that are carried out by the SH2 domains of the Src-family kinases Src and Lck. SA stops the progression of diabetes in diabetic rats fed a high-fat diet and given fibrosis caused by streptozotocin. Hepatic triglyceride (TG) levels are significantly decreased and hyperlipidemia is improved by an oral dose of SA at 0.3 mg/kg twice daily for 16 weeks. In clinical trial NCT03908242, salvanolic acid A is being studied (Phase I Study of Continuous Administration of Salvianolic Acid A Tablet). This substance significantly inhibited the M^{pro} less effectively than its analog rosmarinic acid, with an IC_{50} value of 28.38 μM, which suggests that the extra 3,4-dihydroxy phenyl acrylate unit in salvianolic acid may have caused steric hindrance in binding at the M^{pro} active site.

The concentration−inhibition curves for selected compounds are shown in Figure 8.

Preprints (www.preprints.org) | NOT PEER-REVIEWED | Posted: 28 November 2022 doi:10.20944/preprints202211.0516.v1

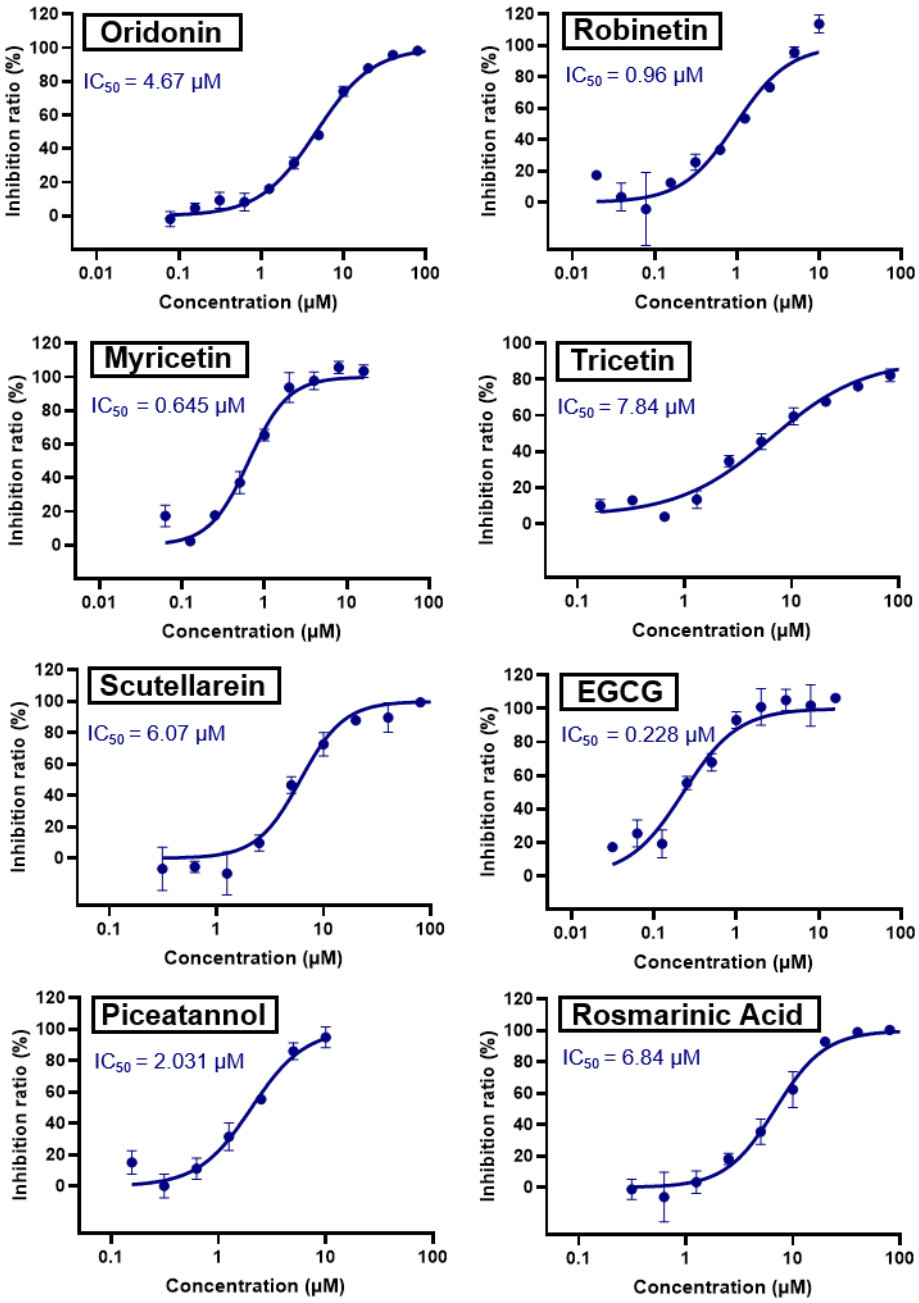

Figure 8. Concentration-dependent inhibition of SARS-CoV-2 M^{pro} by the best inhibitors of the present series: Oridonin, robinetin, myricetin, tricetin, scutellarein, L-epigallocatechin gallate, piceatannol, rosmarinic Acid.

2.2. Cytotoxicity and Anti-SARS-CoV-2 activity

Cytotoxicity. Prior to examining the antiviral activity in Calu-3 cells, selected M^{pro} natural product inhibitors were tested in the cell line at a high concentration of 10 μM for cytotoxicity. No tested substance exhibited cytotoxicity, as shown in Figure S1.

Preprints (www.preprints.org) | NOT PEER-REVIEWED | Posted: 28 November 2022 doi:10.20944/preprints202211.0516.v1

Antiviral activity. The most common method for determining antiviral efficacy against respiratory pathogens in vitro uses the human lung-derived Calu-3 cells, in which SARS-CoV-2 enters the cells in a TMPRSS2-dependent manner. To assess each of the chosen M^{pro} inhibitors, Calu-3 cells were infected with SARS-CoV-2.

Cells were incubated with 10-fold serial dilutions of each inhibitor or DMSO (solvent control) for 1-hour prior infection and for 24 hours after infection (p.i.) with SARS-CoV-2 isolate NK, Pango lineage B.1.513 (kindly provided by Stephan Ludwig, Institute of Virology, University of Münster, Germany) at a multiplicity of infection (MOI) of 0.01. Cell culture supernatants were harvested at 24 h p.i. and titrated on Vero E6 cells to determine viral titers given as plaque-forming units (PFU) per millilitre (Figure S2). The well-known SARS-CoV-2 inhibitor Molnupravir served as the positive control.

Based on these findings, concentration-dependent inhibition curves were generated for all active inhibitors to determine EC_{50} values (Figure 9). All tested compounds showed inhibition of viral titers above 80% at a concentration of 10 µM (Robinetin: 89.6%, Piceatannol: 81.0%, Porsmarinic acid: 81.0%, Scutellarein: 87.0%, EGCG: 81.4, Oridonin: 89%).

EC_{50} values ranged between 1.3 nM (robinetin) and 115 nM (EGCG, Figure 9), which were several fold more potent compared to their MPRO inhibitory activities. These natural products have been reported for several targets, and the inhibition of virus replication in cells might be contributed by the inhibition of non-specific targets as well. Therefore, these inhibitors should be used with caution.

Preprints (www.preprints.org) | NOT PEER-REVIEWED | Posted: 28 November 2022 doi:10.20944/preprints202211.0516.v1

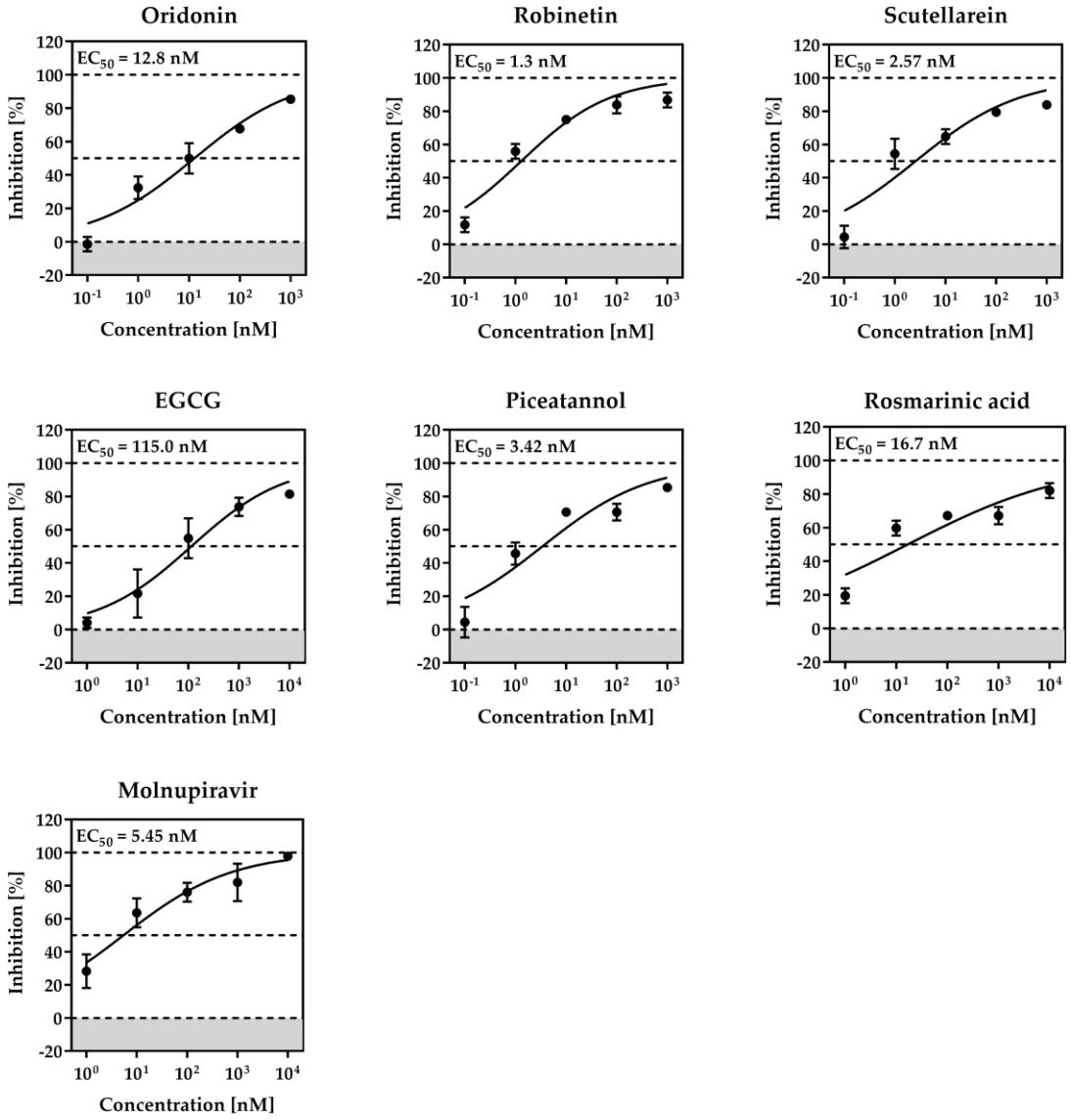

Figure 9: Antiviral activities and cytotoxicities of robinetin, piceatannol, rosmarinic acid, scutellarein, EGCG, oridonin in Calu-3 cells. Calu-3 cells were incubated with 10-fold serial dilutions (10–0.001 or 1-0.0001 μM) of each inhibitor or DMSO (solvent control) for 1 h followed by infection with SARS-CoV-2 at a multiplicity of infection (MOI) of 0.01. After virus inoculation, cells were further incubated with the respective inhibitors for 24 h. Supernatants were harvested, and viral titers were determined by titration on Vero E6 cells. For normalization, viral titers of DMSO-treated cells were set as 0% inhibition. Means ± SDs from three biological replicates are presented.

Preprints (www.preprints.org) | NOT PEER-REVIEWED | Posted: 28 November 2022 doi:10.20944/preprints202211.0516.v1

2.4. Colloidal aggregation assays: In early drug discovery, aggregation is a common reason for false positives when organic [59], drug-like molecules are added to aqueous media and spontaneously form colloidal particles [59–62]. Because proteins are trapped on the colloid surface and partially unfolded there [63], the resulting liquid particles are tightly packed spheres that promiscuously inhibit proteins [64,65]. Due to enzyme crowding on the particle's surface [65], the resulting inhibition is reversible by disrupting the colloid and is characterized by an incubation effect lasting several minutes. Colloids can frequently be broken up by adding non-ionic detergents like Triton X-100 in small amounts, frequently at sub-critical micelle concentrations [66]. Therefore, one frequent perturbation to quickly identify aggregates is to add detergent to counter screens against model enzymes like AmpC β-lactamase or malate dehydrogenase (MDH). Nuclear magnetic resonance (NMR) and dynamic light scattering (DLS) are two well-suited biophysical techniques that can detect aggregation [67], especially with DLS, as the colloids typically form particles in the 50 to 500 nm radius size range.

The Shoichet group recently reported that colloidal aggregation can cause false positive results in studies to reposition drugs against SARS-CoV-2 targets. We chose ECGC and robinetin, two potent natural products, for the current study if they could form colloidal particles. Each substance was initially screened against MDH in triplicate at 31.6 μM. Compounds that demonstrated > 40% enzyme inhibition against MDH were tested in triplicate for detergent reversibility at 31.6 μM with or without 0.01% (v/v) Triton X-100. As previously described, enzymatic reactions were carried

Preprints (www.preprints.org) | NOT PEER-REVIEWED | Posted: 28 November 2022 doi:10.20944/preprints202211.0516.v1

out and observed. Each compound was screened at 31.6 μM on DLS and the critical aggregation concentration (CAC) data for each compound was determined if colloidal particle formation was detected.

The outcomes demonstrated that both EGCG and robinetin had a weak inhibition of MDH with IC_{50}'s of 14.28 and 10.47 μM (Figure 10A,B), whose inhibitions were reversed in the presence of detergent (Figure 10C). However, neither of these compounds produced colloidal-like particles for DLS (Figure 10D) indicating that they can both be categorized as non-specific inhibitors and should be used with caution at concentrations where MDH inhibition was shown.

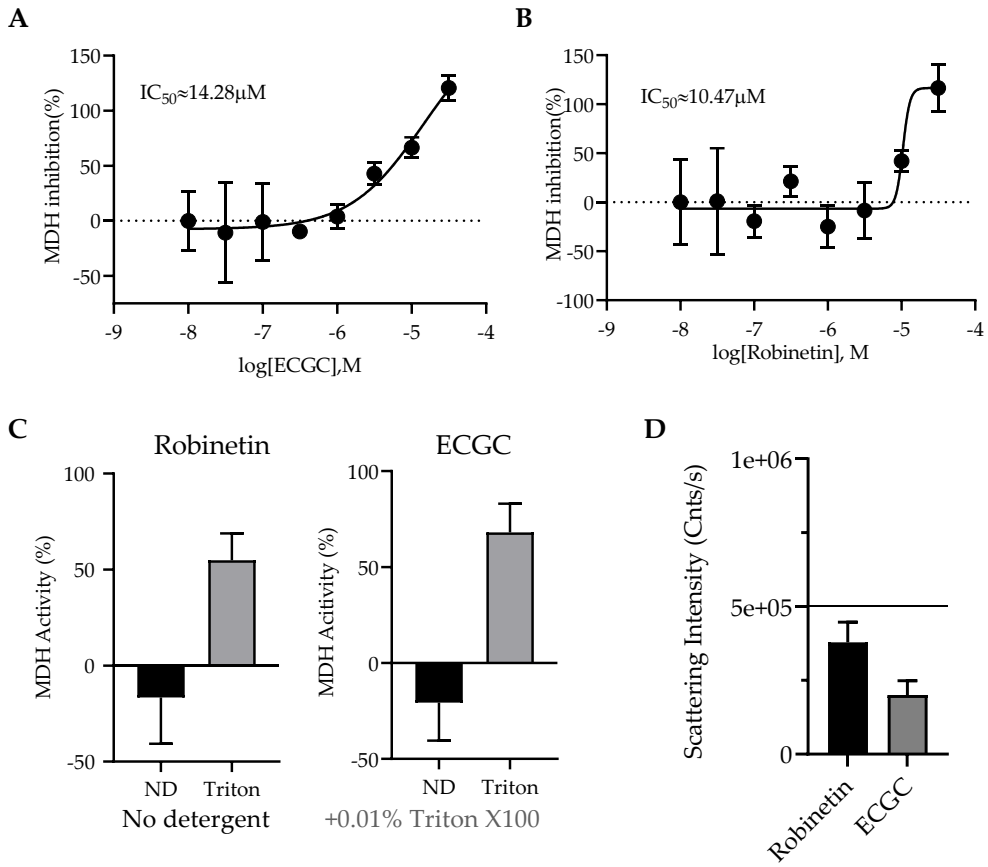

Preprints (www.preprints.org) | NOT PEER-REVIEWED | Posted: 28 November 2022 doi:10.20944/preprints202211.0516.v1

Figure 10. Aggregation assays. Malate dehydrogenase (MDH) enzymatic screen for ECGC (A) and robinetin (B). C) Malate dehydrogenase (MDH) enzymatic activity with or without 0.01% Triton X-100 at 31.6 μM. D) Scattering intensity of compounds PT-69 and Robinetin that do not form colloidal-like particles measured by DLS at 31.6 μM.

3. Materials and Methods

3.1. Compounds

All compounds are >95% pure by HPLC, as reported by the vendors. Compounds were ordered from Sigma-Aldrich, AmBeed, or TCI Europe.

3.2. The inhibition assay of SARS-CoV-2 M^{pro}

The expression and purification of recombinant SARS-CoV-2 M^{pro} were performed as previously reported [22]. A fluorescence resonance energy transfer (FRET) protease assay was applied to measure the inhibitory activity of compounds against the SARS-CoV-2 M^{pro}. The fluorogenic substrate (Dacyl-KTSAVLQSGFRKME-Edans) was synthesized by GenScript (Nanjing, China). The FRET-based protease assay was performed as follows. SARS-CoV-2 M^{pro} (50 nM) was mixed with compounds in assay buffer (50 mM Tris-HCl, pH 7.3, 1 mM EDTA) and incubated for 10 min. The reaction was initiated by adding fluorogenic substrate at a final concentration of 10 μM. Then, the fluorescence signal at 340 nm (excitation)/ 490 nm (emission) was measured every 1 min for 10 min using a Bio-Tek SynergyH1 plate reader. The initial velocities of reactions with compounds added at various concentrations compared to the reaction

Preprints (www.preprints.org) | NOT PEER-REVIEWED | Posted: 28 November 2022 doi:10.20944/preprints202211.0516.v1

added with DMSO were calculated and used to generate inhibitory profile curves for IC_{50} determination.

3.3. Dynamic Light Scattering (DLS)

Samples were prepared in filtered 50 mM KPi buffer, pH 7.0 with final DMSO concentration at 1% (v/v). Colloidal particle formation was detected using DynaPro Plate Reader II (Wyatt Technologies). All compounds were screened in triplicate at 31.6μM and, if colloids were detected, 8-point half-log dilutions of compounds were performed on DLS in triplicate. To determine the critical aggregation concentration (CAC), data for each compound were spilt into two data sets based on aggregating (*i.e.* $>10^6$ scattering intensity) and non- aggregating (*i.e.* $<10^6$ scattering intensity) and were fitted with separate nonlinear regression curves, and the point of intersection was determined using GraphPad Prism software version 9.1.1 (San Diego, CA).

3.4. Malate dehydrogenase inhibition assays

Enzyme inhibition assays were performed at room temperature using CLARIOstar Plate Reader (BMG Labtech). Samples were prepared in 50 mM KPi buffer, pH 7.0 with final DMSO concentration at 1% (v/v). Compounds were incubated with 2 nM Malate dehydrogenase (MDH) for 5 minutes. MDH reactions were initiated by the addition of 200 μM nicotinamide adenine dinucleotide (NADH) (54839, Sigma Aldrich) and 200 μM oxaloacetic acid (324427, Sigma Aldrich). The change in absorbance was monitored at 340 nm for 1 min 30 sec. Initial rates were divided by

 doi:10.20944/preprints202211.0516.v1

the DMSO control rate to determine % enzyme activity. Each compound was screened at 31.6 μM in triplicate. Data was analyzed using GraphPad Prism software version 9.1.1 (San Diego, CA).

For detergent reversibility, compounds that showed > 40% enzyme inhibition against MDH were screened at 31.6 μM with or without 0.01% (v/v) Triton X-100 in triplicate. Enzymatic reactions were performed/monitored as previously described.

3.5. Cytotoxicity and antiviral assays

Cell Vitality Assay. To determine cell vitality of Calu-3 cells treated with inhibitors, the CellTiter-Glo Luminescent Cell Viability Assay Kit (Promega) was used. Cells were grown in 96-well plates until reaching 50−60% confluency before they were incubated with DMSO (solvent control) or M^{pro} inhibitors at a concentration of 10 μM for 24 h. Next, cell culture supernatants were removed, and 50 μL of the CellTiter-Glo substrate was added to each well and incubated for 30 min on a rocking platform. Finally, samples were transferred into white 96-well plates, and luminescence was measured using a Hidex Sense plate luminometer (Hidex).

Antiviral Activity. All work with infectious SARS-CoV-2 was conducted under BSL-3 conditions at the German Primate Centre, Göttingen/Germany. Calu-3 cells were grown in 48-well plates until reaching approx. 70% confluency. Cells were incubated with 10-fold serial dilutions (10−0.001 or 1-0.0001 μM) of M^{pro} inhibitors for 1 h at 37 °C prior infections. Next, the inhibitor containing the cell culture medium was removed, and cells were infected with SARS-CoV-2 isolate NK, Pango lineage B.1.513, at an MOI

Preprints (www.preprints.org) | NOT PEER-REVIEWED | Posted: 28 November 2022 doi:10.20944/preprints202211.0516.v1

of 0.01 in an inoculum volume of 400 µL for 1 h at 37 °C. At 1 h post infection (p.i.), the inoculum was removed, cells were washed with PBS three times and further incubated in a cell culture medium containing the respective inhibitor for 24 h. Virus containing supernatants were harvested and stored at −80 °C until further usage. Viral titers were determined by titration on VeroE6 cells and methylcellulose overlay.

3.6. Molecular modelling

Three-dimensional ligand structures were generated with LigPrep (implemented in Maestro 2021v4), using Epik to predict their protonation in pH 7.0 ± 2.0, and generating tautomers and diastereoisomers [68]. The OPLS4 force-field was employed for structure generation [69]. The SARS-CoV-2 M^{pro} protein structure was previously prepared from the PDB 7DPP, using the Protein Wizard Preparation tool, with standard options. Covalent docking as performed using CovDock [70] using the Cys145 as anchor, nucleophilic addition to double bond or Michael addition as reaction types and generating up to 10 poses for each ligand, best scored pose was selected and figures were generated using PyMOL 2.5.2.

3.7. X-ray protein crystallography experiments

The purified SARS-CoV-2 M^{pro} protein was concentrated to 9 mg/mL for crystallization. To obtain complex structures, the SARS-CoV-2 M^{pro} protein was incubated with 1 mM Robinetin before crystallization condition screening. Crystallization was performed at 20 ℃ using a hanging drop vapor-diffusion method

Preprints (www.preprints.org) | NOT PEER-REVIEWED | Posted: 28 November 2022 doi:10.20944/preprints202211.0516.v1

by mixing equal volumes (1:1 μL) of the M^{pro}-Robinetin mixture and reservoir solution. Crystals of the complex were obtained under the condition of 10-25% PEG6000, 100 mM MES, pH 5.5-6.75, and 3% DMSO. Crystals were flash frozen in liquid nitrogen in the presence of the reservoir solution supplemented with 20% glycerol. X-ray diffraction data were collected at beamline BL19U1 at the Shanghai Synchrotron Radiation Facility [71]. The complex structures were solved by molecular replacement using the program PHASER [72] with a search model of PDB code 6M2N. The model was built using Coot [73] and refined with XYZ (reciprocal-space), Individual B factors, TLS parameters, and Occupancies implemented in the program PHENIX [74]. The refined structures were deposited to Protein Data Bank with the PDB code of 8HI9. The complete statistics as well as the quality of the solved structures are also shown in Table 1.

Table 1. Crystallography data collection and refinement statistics.

	SARS-CoV-2 M^{pro}-Robinetin
PDB ID	8HI9
Space Group	P 21
Cell Dimension: a (Å)	44.156
b (Å)	54.182
c (Å)	115.416
Wavelength (Å)	0.979
Reflections (unique)	24333
Resolution Range (Å)	2.28-37.78
Highest-Resolution Shell (Å)	2.28-2.39
Redundancy	6.1(6.2)

Preprints (www.preprints.org) | NOT PEER-REVIEWED | Posted: 28 November 2022 doi:10.20944/preprints202211.0516.v1

I/σ (I)	14.8(6.9)
Completeness (%)	99.0(99.0)
Rwork/Rfree	0.2457/0.2553
Clashscore	1.72
MolProbity Score	0.93
RMS Values	
Bond length (Å)	0.003
Bond angle (°)	0.638
Numbers of Non-hydrogen Atoms	
Protein	4449
Inhibitor	44
Water Oxygen	108
Others	0
B-factor (Å^2)	
Protein	33.33
Inhibitor	35.13
Water Oxygen	29.42
Ramachandran plot	
Favored (%)	98.32
Allowed (%)	1.52
Outliers (%)	0.17

4. Conclusions

New chemical phenotypes are commonly found in natural goods. In the current work, we evaluated 31 natural compounds and their derivatives that may be SARS-CoV-2 M^{pro} inhibitors. Ten of them were shown to be M^{pro} inhibitors. Roninetin, rosmarinic acid, and its derivative salvianolic acid A were shown to be novel M^{pro} ligands, and the M^{pro} inhibitory was reinforced for myricetin, oridonin, scutellarein, and L-epigallocatechin gallate. Utilizing molecular docking studies, the binding mode of

 doi:10.20944/preprints202211.0516.v1

potent M^{pro} inhibitors was investigated. Additionally, the structural determination of robinetin with M^{pro} provided rational for new analogues design. The strong antiviral activity of the selected potent compounds, especially robinetin with an EC_{50} of 1.3 nM, indicates promising options for further research as an antiviral therapy for COVID-19.

Supplementary Materials: The following supporting information can be downloaded at: **Figure S1.** Cell vitality of Calu-3 cells treated with M^{pro} inhibitors; **Figure 2**. Antiviral activity of M^{pro} inhibitors on SARS-CoV-2 infectivity in Calu-3 cells.

Author Contributions: Conceptualization, T.P and S.L.; M^{pro} inhibitory activities, Y.X. H. S.; Antiviral testing, N.K. and XX.; DLS and MDH assays, I.G. J. O. and B.K.S.; computational studies, T.K.; writing-original draft preparation, T.P.; writing-review and editing, T.P. S.L. T.K, Y.X. and B.K.S. All authors have read and agreed to the published version of the manuscript.

Acknowledgements

TüCAD2 is funded by the Federal Ministry of Education and Research (BMBF) and the Baden-Württemberg Ministry of Science as part of the Excellence Strategy of the German Federal and State Governments EXC 2180–390900677 T.K. is supported by the Fortüne initiative (Nr. 2613-0-0) and by the iFIT, which are both initiatives from the Excellence Strategy of the German Federal and State Governments. The authors would like to thank the CSC – Finland for the generous computational resources provided. We thank Isabella Glenn (Shoichet group, UCSF) for assistance with DLS and malate dehydrogenase studies of Robinetin and ECGC (PT-69)", and thank the staff from BL19U beamline of National Facility for Protein Science in Shanghai (NFPS) at

Shanghai Synchrotron Radiation Facility for assistance during data collection. This work was supported by the Science and Technology Commission of Shanghai Municipality (No. 20430780300) and the Qiusuo Outstanding Youth Project of Lingang Laboratory (No. LG-QS-202205-02).

Funding: Not applicable.

Institutional Review Board Statement: Not applicable.

Informed Consent Statement: Not applicable.

Data Availability Statement: Data is contained within the article and supplementary material.

Conflicts of Interest: The authors declare no conflict of interest.

References

1. Ll, W.; M, M.; M, E.; Pillaiyar, T. The Recent Outbreaks of Human Coronaviruses: A Medicinal Chemistry Perspective. *Med. Res. Rev.* **2021**, *41*, doi:10.1002/med.21724.
2. Zhou, P.; Yang, X.-L.; Wang, X.-G.; Hu, B.; Zhang, L.; Zhang, W.; Si, H.-R.; Zhu, Y.; Li, B.; Huang, C.-L.; et al. Addendum: A Pneumonia Outbreak Associated with a New Coronavirus of Probable Bat Origin. *Nature* **2020**, *588*, E6, doi:10.1038/s41586-020-2951-z.
3. Li, Q.; Guan, X.; Wu, P.; Wang, X.; Zhou, L.; Tong, Y.; Ren, R.; Leung, K.S.M.; Lau, E.H.Y.; Wong, J.Y.; et al. Early Transmission Dynamics in Wuhan, China, of Novel Coronavirus–Infected Pneumonia. *N. Engl. J. Med.* **2020**, *382*, 1199–1207, doi:10.1056/NEJMoa2001316.
4. Chan, J.F.-W.; Yuan, S.; Kok, K.-H.; To, K.K.-W.; Chu, H.; Yang, J.; Xing, F.; Liu, J.; Yip, C.C.-Y.; Poon, R.W.-S.; et al. A Familial Cluster of Pneumonia Associated with the 2019 Novel Coronavirus Indicating Person-to-Person Transmission: A Study of a Family Cluster. *The Lancet* **2020**, *395*, 514–523, doi:10.1016/S0140-6736(20)30154-9.
5. Dai, W.; Zhang, B.; Jiang, X.-M.; Su, H.; Li, J.; Zhao, Y.; Xie, X.; Jin, Z.; Peng, J.; Liu, F.; et al. Structure-Based Design of Antiviral Drug Candidates Targeting the SARS-CoV-2 Main Protease. *Science* **2020**, *368*, 1331–1335, doi:10.1126/science.abb4489.

6. Mellott, D.M.; Tseng, C.-T.; Drelich, A.; Fajtová, P.; Chenna, B.C.; Kostomiris, D.H.; Hsu, J.; Zhu, J.; Taylor, Z.W.; Kocurek, K.I.; et al. A Clinical-Stage Cysteine Protease Inhibitor Blocks SARS-CoV-2 Infection of Human and Monkey Cells. *ACS Chem. Biol.* **2021**, *16*, 642–650, doi:10.1021/acschembio.0c00875.
7. Zhang, L.; Lin, D.; Sun, X.; Curth, U.; Drosten, C.; Sauerhering, L.; Becker, S.; Rox, K.; Hilgenfeld, R. Crystal Structure of SARS-CoV-2 Main Protease Provides a Basis for Design of Improved α-Ketoamide Inhibitors. *Science* **2020**, *368*, 409–412, doi:10.1126/science.abb3405.
8. Konno, S.; Kobayashi, K.; Senda, M.; Funai, Y.; Seki, Y.; Tamai, I.; Schäkel, L.; Sakata, K.; Pillaiyar, T.; Taguchi, A.; et al. 3CL Protease Inhibitors with an Electrophilic Arylketone Moiety as Anti-SARS-CoV-2 Agents. *J. Med. Chem.* **2022**, *65*, 2926–2939, doi:10.1021/acs.jmedchem.1c00665.
9. Ghosh, A.K.; Kovela, S.; Osswald, H.L.; Amano, M.; Aoki, M.; Agniswamy, J.; Wang, Y.-F.; Weber, I.T.; Mitsuya, H. Structure-Based Design of Highly Potent HIV-1 Protease Inhibitors Containing New Tricyclic Ring P2-Ligands: Design, Synthesis, Biological, and X-Ray Structural Studies. *J. Med. Chem.* **2020**, *63*, 4867–4879, doi:10.1021/acs.jmedchem.0c00202.
10. Boras, B.; Jones, R.M.; Anson, B.J.; Arenson, D.; Aschenbrenner, L.; Bakowski, M.A.; Beutler, N.; Binder, J.; Chen, E.; Eng, H.; et al. Preclinical Characterization of an Intravenous Coronavirus 3CL Protease Inhibitor for the Potential Treatment of COVID19. *Nat. Commun.* **2021**, *12*, 6055, doi:10.1038/s41467-021-26239-2.
11. Pillaiyar, T.; Meenakshisundaram, S.; Manickam, M. Recent Discovery and Development of Inhibitors Targeting Coronaviruses. *Drug Discov. Today* **2020**, *25*, 668–688, doi:10.1016/j.drudis.2020.01.015.
12. Pillaiyar, T.; Manickam, M.; Namasivayam, V.; Hayashi, Y.; Jung, S.-H. An Overview of Severe Acute Respiratory Syndrome–Coronavirus (SARS-CoV) 3CL Protease Inhibitors: Peptidomimetics and Small Molecule Chemotherapy. *J. Med. Chem.* **2016**, *59*, 6595–6628, doi:10.1021/acs.jmedchem.5b01461.
13. de Wit, E.; van Doremalen, N.; Falzarano, D.; Munster, V.J. SARS and MERS: Recent Insights into Emerging Coronaviruses. *Nat. Rev. Microbiol.* **2016**, *14*, 523–534, doi:10.1038/nrmicro.2016.81.
14. Muramatsu, T.; Takemoto, C.; Kim, Y.-T.; Wang, H.; Nishii, W.; Terada, T.; Shirouzu, M.; Yokoyama, S. SARS-CoV 3CL Protease Cleaves Its C-Terminal Autoprocessing Site by Novel Subsite Cooperativity. *Proc. Natl. Acad. Sci. U. S. A.* **2016**, *113*, 12997–13002, doi:10.1073/pnas.1601327113.
15. Anand, P.; Kunnumakkara, A.B.; Newman, R.A.; Aggarwal, B.B. Bioavailability of Curcumin: Problems and Promises. *Mol. Pharm.* **2007**, *4*, 807–818, doi:10.1021/mp700113r.
16. Yang, H.; Xie, W.; Xue, X.; Yang, K.; Ma, J.; Liang, W.; Zhao, Q.; Zhou, Z.; Pei, D.; Ziebuhr, J.; et al. Design of Wide-Spectrum Inhibitors Targeting Coronavirus Main Proteases. *PLOS Biol.* **2005**, *3*, e324, doi:10.1371/journal.pbio.0030324.

17. Zumla, A.; Chan, J.F.W.; Azhar, E.I.; Hui, D.S.C.; Yuen, K.-Y. Coronaviruses - Drug Discovery and Therapeutic Options. *Nat. Rev. Drug Discov.* **2016**, *15*, 327–347, doi:10.1038/nrd.2015.37.
18. Jin, Z.; Zhao, Y.; Sun, Y.; Zhang, B.; Wang, H.; Wu, Y.; Zhu, Y.; Zhu, C.; Hu, T.; Du, X.; et al. Structural Basis for the Inhibition of SARS-CoV-2 Main Protease by Antineoplastic Drug Carmofur. *Nat. Struct. Mol. Biol.* **2020**, *27*, 529–532, doi:10.1038/s41594-020-0440-6.
19. Al-Harrasi, A.; Behl, T.; Upadhyay, T.; Chigurupati, S.; Bhatt, S.; Sehgal, A.; Bhatia, S.; Singh, S.; Sharma, N.; Vijayabalan, S.; et al. Targeting Natural Products against SARS-CoV-2. *Environ. Sci. Pollut. Res.* **2022**, *29*, 42404–42432, doi:10.1007/s11356-022-19770-2.
20. Li, S.-Y.; Chen, C.; Zhang, H.-Q.; Guo, H.-Y.; Wang, H.; Wang, L.; Zhang, X.; Hua, S.-N.; Yu, J.; Xiao, P.-G.; et al. Identification of Natural Compounds with Antiviral Activities against SARS-Associated Coronavirus. *Antiviral Res.* **2005**, *67*, 18–23, doi:10.1016/j.antiviral.2005.02.007.
21. Su, H.; Yao, S.; Zhao, W.; Zhang, Y.; Liu, J.; Shao, Q.; Wang, Q.; Li, M.; Xie, H.; Shang, W.; et al. Identification of Pyrogallol as a Warhead in Design of Covalent Inhibitors for the SARS-CoV-2 3CL Protease. *Nat. Commun.* **2021**, *12*, 3623, doi:10.1038/s41467-021-23751-3.
22. Su, H.-X.; Yao, S.; Zhao, W.-F.; Li, M.-J.; Liu, J.; Shang, W.-J.; Xie, H.; Ke, C.-Q.; Hu, H.-C.; Gao, M.-N.; et al. Anti-SARS-CoV-2 Activities in Vitro of Shuanghuanglian Preparations and Bioactive Ingredients. *Acta Pharmacol. Sin.* **2020**, *41*, 1167–1177, doi:10.1038/s41401-020-0483-6.
23. Miyazawa, M.; Nakamura, Y.; Ishikawa, Y. Insecticidal Sesquiterpene from Alpinia Oxyphylla against Drosophila Melanogaster. *J. Agric. Food Chem.* **2000**, *48*, 3639–3641, doi:10.1021/jf000325z.
24. Biolatto, A.; Sancho, A.M.; Cantet, R.J.C.; Güemes, D.R.; Pensel, N.A. Use of Nootkatone as a Senescence Indicator for Rouge La Toma Cv. Grapefruit (Citrus Paradisi Macf.). *J. Agric. Food Chem.* **2002**, *50*, 4816–4819, doi:10.1021/jf011674b.
25. Kadota, S.; Basnet, P.; Ishii, E.; Tamura, T.; Namba, T. Antibacterial Activity of Trichorabdal A from Rabdosia Trichocarpa against Helicobacter Pylori. *Zentralblatt Bakteriol. Int. J. Med. Microbiol.* **1997**, *286*, 63–67, doi:10.1016/s0934-8840(97)80076-x.
26. Kuo, L.-M.; Kuo, C.-Y.; Lin, C.-Y.; Hung, M.-F.; Shen, J.-J.; Hwang, T.-L. Intracellular Glutathione Depletion by Oridonin Leads to Apoptosis in Hepatic Stellate Cells. *Mol. Basel Switz.* **2014**, *19*, 3327–3344, doi:10.3390/molecules19033327.
27. Huang, J.; Wu, L.; Tashiro, S.-I.; Onodera, S.; Ikejima, T. A Comparison of the Signal Pathways between the TNF Alpha- and Oridonin-Induced Murine L929 Fibrosarcoma Cell Death. *Acta Med. Okayama* **2005**, *59*, 261–270, doi:10.18926/AMO/31960.
28. Xu, Y.; Xue, Y.; Wang, Y.; Feng, D.; Lin, S.; Xu, L. Multiple-Modulation Effects of Oridonin on the Production of Proinflammatory Cytokines and Neurotrophic

Factors in LPS-Activated Microglia. *Int. Immunopharmacol.* **2009**, *9*, 360–365, doi:10.1016/j.intimp.2009.01.002.

29. Zhao, G.; Zhang, T.; Ma, X.; Jiang, K.; Wu, H.; Qiu, C.; Guo, M.; Deng, G. Oridonin Attenuates the Release of Pro-Inflammatory Cytokines in Lipopolysaccharide-Induced RAW264.7 Cells and Acute Lung Injury. *Oncotarget* **2017**, *8*, 68153–68164, doi:10.18632/oncotarget.19249.
30. Song, M.; Liu, X.; Liu, K.; Zhao, R.; Huang, H.; Shi, Y.; Zhang, M.; Zhou, S.; Xie, H.; Chen, H.; et al. Targeting AKT with Oridonin Inhibits Growth of Esophageal Squamous Cell Carcinoma In Vitro and Patient-Derived Xenografts In Vivo. *Mol. Cancer Ther.* **2018**, *17*, 1540–1553, doi:10.1158/1535-7163.MCT-17-0823.
31. He, H.; Jiang, H.; Chen, Y.; Ye, J.; Wang, A.; Wang, C.; Liu, Q.; Liang, G.; Deng, X.; Jiang, W.; et al. Oridonin Is a Covalent NLRP3 Inhibitor with Strong Anti-Inflammasome Activity. *Nat. Commun.* **2018**, *9*, 2550, doi:10.1038/s41467-018-04947-6.
32. Zhong, B.; Peng, W.; Du, S.; Chen, B.; Feng, Y.; Hu, X.; Lai, Q.; Liu, S.; Zhou, Z.-W.; Fang, P.; et al. Oridonin Inhibits SARS-CoV-2 by Targeting Its 3C-Like Protease. *Small Sci.* **2022**, *2*, 2270012, doi:10.1002/smsc.202270012.
33. Birt, D.F.; Walker, B.; Tibbels, M.G.; Bresnick, E. Anti-Mutagenesis and Anti-Promotion by Apigenin, Robinetin and Indole-3-Carbinol. *Carcinogenesis* **1986**, *7*, 959–963, doi:10.1093/carcin/7.6.959.
34. Chang, R.L.; Huang, M.T.; Wood, A.W.; Wong, C.Q.; Newmark, H.L.; Yagi, H.; Sayer, J.M.; Jerina, D.M.; Conney, A.H. Effect of Ellagic Acid and Hydroxylated Flavonoids on the Tumorigenicity of Benzo[a]Pyrene and (+/-)-7 Beta, 8 Alpha-Dihydroxy-9 Alpha, 10 Alpha-Epoxy-7,8,9,10-Tetrahydrobenzo[a]Pyrene on Mouse Skin and in the Newborn Mouse. *Carcinogenesis* **1985**, *6*, 1127–1133, doi:10.1093/carcin/6.8.1127.
35. Kyaw, M.; Yoshizumi, M.; Tsuchiya, K.; Izawa, Y.; Kanematsu, Y.; Tamaki, T. Atheroprotective Effects of Antioxidants through Inhibition of Mitogen-Activated Protein Kinases. *Acta Pharmacol. Sin.* **2004**, *25*, 977–985.
36. Mahmud, S.; Uddin, M.A.R.; Paul, G.K.; Shimu, M.S.S.; Islam, S.; Rahman, E.; Islam, A.; Islam, M.S.; Promi, M.M.; Emran, T.B.; et al. Virtual Screening and Molecular Dynamics Simulation Study of Plant-Derived Compounds to Identify Potential Inhibitors of Main Protease from SARS-CoV-2. *Brief. Bioinform.* **2021**, *22*, 1402–1414, doi:10.1093/bib/bbaa428.
37. Ren, J.; Yuan, L.; Wang, W.; Zhang, M.; Wang, Q.; Li, S.; Zhang, L.; Hu, K. Tricetin Protects against 6-OHDA-Induced Neurotoxicity in Parkinson's Disease Model by Activating Nrf2/HO-1 Signaling Pathway and Preventing Mitochondria-Dependent Apoptosis Pathway. *Toxicol. Appl. Pharmacol.* **2019**, *378*, 114617, doi:10.1016/j.taap.2019.114617.
38. Wu, Q.; Yan, S.; Wang, Y.; Li, M.; Xiao, Y.; Li, Y. Discovery of 4'-O-Methylscutellarein as a Potent SARS-CoV-2 Main Protease Inhibitor. *Biochem. Biophys. Res. Commun.* **2022**, *604*, 76–82, doi:10.1016/j.bbrc.2022.03.052.

39. Liu, H.; Ye, F.; Sun, Q.; Liang, H.; Li, C.; Li, S.; Lu, R.; Huang, B.; Tan, W.; Lai, L. Scutellaria Baicalensis Extract and Baicalein Inhibit Replication of SARS-CoV-2 and Its 3C-like Protease in Vitro. *J. Enzyme Inhib. Med. Chem.* **2021**, *36*, 497–503, doi:10.1080/14756366.2021.1873977.
40. Xing, L.; Zhang, H.; Qi, R.; Tsao, R.; Mine, Y. Recent Advances in the Understanding of the Health Benefits and Molecular Mechanisms Associated with Green Tea Polyphenols. *J. Agric. Food Chem.* **2019**, *67*, 1029–1043, doi:10.1021/acs.jafc.8b06146.
41. Jang, M.; Park, Y.-I.; Cha, Y.-E.; Park, R.; Namkoong, S.; Lee, J.I.; Park, J. Tea Polyphenols EGCG and Theaflavin Inhibit the Activity of SARS-CoV-2 3CL-Protease In Vitro. *Evid.-Based Complement. Altern. Med. ECAM* **2020**, *2020*, 5630838, doi:10.1155/2020/5630838.
42. Zuo, G.; Li, Z.; Chen, L.; Xu, X. Activity of Compounds from Chinese Herbal Medicine Rhodiola Kirilowii (Regel) Maxim against HCV NS3 Serine Protease. *Antiviral Res.* **2007**, *76*, 86–92, doi:10.1016/j.antiviral.2007.06.001.
43. Nguyen, T.T.H.; Woo, H.-J.; Kang, H.-K.; Nguyen, V.D.; Kim, Y.-M.; Kim, D.-W.; Ahn, S.-A.; Xia, Y.; Kim, D. Flavonoid-Mediated Inhibition of SARS Coronavirus 3C-like Protease Expressed in Pichia Pastoris. *Biotechnol. Lett.* **2012**, *34*, 831–838, doi:10.1007/s10529-011-0845-8.
44. Du, A.; Zheng, R.; Disoma, C.; Li, S.; Chen, Z.; Li, S.; Liu, P.; Zhou, Y.; Shen, Y.; Liu, S.; et al. Epigallocatechin-3-Gallate, an Active Ingredient of Traditional Chinese Medicines, Inhibits the 3CLpro Activity of SARS-CoV-2. *Int. J. Biol. Macromol.* **2021**, *176*, 1–12, doi:10.1016/j.ijbiomac.2021.02.012.
45. Chiou, W.-C.; Chen, J.-C.; Chen, Y.-T.; Yang, J.-M.; Hwang, L.-H.; Lyu, Y.-S.; Yang, H.-Y.; Huang, C. The Inhibitory Effects of PGG and EGCG against the SARS-CoV-2 3C-like Protease. *Biochem. Biophys. Res. Commun.* **2022**, *591*, 130–136, doi:10.1016/j.bbrc.2020.12.106.
46. Pillaiyar, T.; Laufer, S. Kinases as Potential Therapeutic Targets for Anti-Coronaviral Therapy. *J. Med. Chem.* **2022**, *65*, 955–982, doi:10.1021/acs.jmedchem.1c00335.
47. Menegazzi, M.; Mariotto, S.; Dal Bosco, M.; Darra, E.; Vaiana, N.; Shoji, K.; Safwat, A.-A.; Marechal, J.D.; Perahia, D.; Suzuki, H.; et al. Direct Interaction of Natural and Synthetic Catechins with Signal Transducer Activator of Transcription 1 Affects Both Its Phosphorylation and Activity. *FEBS J.* **2014**, *281*, 724–738, doi:10.1111/febs.12618.
48. Menegazzi, M.; Campagnari, R.; Bertoldi, M.; Crupi, R.; Di Paola, R.; Cuzzocrea, S. Protective Effect of Epigallocatechin-3-Gallate (EGCG) in Diseases with Uncontrolled Immune Activation: Could Such a Scenario Be Helpful to Counteract COVID-19? *Int. J. Mol. Sci.* **2020**, *21*, 5171, doi:10.3390/ijms21145171.
49. Joo, S.-Y.; Song, Y.-A.; Park, Y.-L.; Myung, E.; Chung, C.-Y.; Park, K.-J.; Cho, S.-B.; Lee, W.-S.; Kim, H.-S.; Rew, J.-S.; et al. Epigallocatechin-3-Gallate Inhibits LPS-Induced NF-KB and MAPK Signaling Pathways in Bone Marrow-Derived Macrophages. *Gut Liver* **2012**, *6*, 188–196, doi:10.5009/gnl.2012.6.2.188.

50. Yang, F.; Oz, H.S.; Barve, S.; Villiers, W.J.S. de; McClain, C.J.; Varilek, G.W. The Green Tea Polyphenol (−)-Epigallocatechin-3-Gallate Blocks Nuclear Factor-KB Activation by Inhibiting IκB Kinase Activity in the Intestinal Epithelial Cell Line IEC-6. *Mol. Pharmacol.* **2001**, *60*, 528–533.
51. Almatroodi, S.A.; Almatroudi, A.; Khan, A.A.; Alhumaydhi, F.A.; Alsahli, M.A.; Rahmani, A.H. Potential Therapeutic Targets of Epigallocatechin Gallate (EGCG), the Most Abundant Catechin in Green Tea, and Its Role in the Therapy of Various Types of Cancer. *Mol. Basel Switz.* **2020**, *25*, E3146, doi:10.3390/molecules25143146.
52. Münzenberger, B.; Heilemann, J.; Strack, D.; Kottke, I.; Oberwinkler, F. Phenolics of Mycorrhizas and Non-Mycorrhizal Roots of Norway Spruce. *Planta* **1990**, *182*, 142–148, doi:10.1007/BF00239996.
53. Geahlen, R.L.; McLaughlin, J.L. Piceatannol (3,4,3′,5′-Tetrahydroxy-Trans-Stilbene) Is a Naturally Occurring Protein-Tyrosine Kinase Inhibitor. *Biochem. Biophys. Res. Commun.* **1989**, *165*, 241–245, doi:10.1016/0006-291x(89)91060-7.
54. Scarpati, M.L. Oriente, G. Isolamento e Costituzione Dell'acido Rosmarinico (Dal Rosmarinus Off.). *Ric Sci* **1958**, *28*, 2329–2333.
55. Al-Dhabi, N.A.; Arasu, M.V.; Park, C.H.; Park, S.U. Recent Studies on Rosmarinic Acid and Its Biological and Pharmacological Activities. *EXCLI J.* **2014**, *13*, 1192–1195.
56. Guan, H.; Luo, W.; Bao, B.; Cao, Y.; Cheng, F.; Yu, S.; Fan, Q.; Zhang, L.; Wu, Q.; Shan, M. A Comprehensive Review of Rosmarinic Acid: From Phytochemistry to Pharmacology and Its New Insight. *Molecules* **2022**, *27*, 3292, doi:10.3390/molecules27103292.
57. May, G.; Willuhn, G. [Antiviral effect of aqueous plant extracts in tissue culture]. *Arzneimittelforschung.* **1978**, *28*, 1–7.
58. Häusler, E.; Petersen, M.; Alfermann, A.W. Isolation of Protoplasts and Vacuoles from Cell Suspension Cultures of Coleus Blumei Benth. *Plant Cell Rep.* **1993**, *12*, 510–512, doi:10.1007/BF00236097.
59. McGovern, S.L.; Shoichet, B.K. Kinase Inhibitors: Not Just for Kinases Anymore. *J. Med. Chem.* **2003**, *46*, 1478–1483, doi:10.1021/jm020427b.
60. Doak, A.K.; Wille, H.; Prusiner, S.B.; Shoichet, B.K. Colloid Formation by Drugs in Simulated Intestinal Fluid. *J. Med. Chem.* **2010**, *53*, 4259–4265, doi:10.1021/jm100254w.
61. Seidler, J.; McGovern, S.L.; Doman, T.N.; Shoichet, B.K. Identification and Prediction of Promiscuous Aggregating Inhibitors among Known Drugs. *J. Med. Chem.* **2003**, *46*, 4477–4486, doi:10.1021/jm030191r.
62. Ganesh, A.N.; Donders, E.N.; Shoichet, B.K.; Shoichet, M.S. Colloidal Aggregation: From Screening Nuisance to Formulation Nuance. *Nano Today* **2018**, *19*, 188–200, doi:10.1016/j.nantod.2018.02.011.
63. Coan, K.E.D.; Maltby, D.A.; Burlingame, A.L.; Shoichet, B.K. Promiscuous Aggregate-Based Inhibitors Promote Enzyme Unfolding. *J. Med. Chem.* **2009**, *52*, 2067–2075, doi:10.1021/jm801605r.

64. Blevitt, J.M.; Hack, M.D.; Herman, K.L.; Jackson, P.F.; Krawczuk, P.J.; Lebsack, A.D.; Liu, A.X.; Mirzadegan, T.; Nelen, M.I.; Patrick, A.N.; et al. Structural Basis of Small-Molecule Aggregate Induced Inhibition of a Protein-Protein Interaction. *J. Med. Chem.* **2017**, *60*, 3511–3517, doi:10.1021/acs.jmedchem.6b01836.
65. McGovern, S.L.; Helfand, B.T.; Feng, B.; Shoichet, B.K. A Specific Mechanism of Nonspecific Inhibition. *J. Med. Chem.* **2003**, *46*, 4265–4272, doi:10.1021/jm030266r.
66. Feng, B.Y.; Toyama, B.H.; Wille, H.; Colby, D.W.; Collins, S.R.; May, B.C.H.; Prusiner, S.B.; Weissman, J.; Shoichet, B.K. Small-Molecule Aggregates Inhibit Amyloid Polymerization. *Nat. Chem. Biol.* **2008**, *4*, 197–199, doi:10.1038/nchembio.65.
67. LaPlante, S.R.; Aubry, N.; Bolger, G.; Bonneau, P.; Carson, R.; Coulombe, R.; Sturino, C.; Beaulieu, P.L. Monitoring Drug Self-Aggregation and Potential for Promiscuity in off-Target in Vitro Pharmacology Screens by a Practical NMR Strategy. *J. Med. Chem.* **2013**, *56*, 7073–7083, doi:10.1021/jm4008714.
68. Shelley, J.C.; Cholleti, A.; Frye, L.L.; Greenwood, J.R.; Timlin, M.R.; Uchimaya, M. Epik: A Software Program for PKaprediction and Protonation State Generation for Drug-like Molecules. *J. Comput. Aided Mol. Des.* **2007**, *21*, 681–691, doi:10.1007/s10822-007-9133-z.
69. Lu, C.; Wu, C.; Ghoreishi, D.; Chen, W.; Wang, L.; Damm, W.; Ross, G.A.; Dahlgren, M.K.; Russell, E.; Von Bargen, C.D.; et al. OPLS4: Improving Force Field Accuracy on Challenging Regimes of Chemical Space. *J. Chem. Theory Comput.* **2021**, *17*, 4291–4300, doi:10.1021/acs.jctc.1c00302.
70. Zhu, K.; Borrelli, K.W.; Greenwood, J.R.; Day, T.; Abel, R.; Farid, R.S.; Harder, E. Docking Covalent Inhibitors: A Parameter Free Approach to Pose Prediction and Scoring. *J. Chem. Inf. Model.* **2014**, *54*, 1932–1940, doi:10.1021/ci500118s.
71. Wang, Q.-S.; Zhang, K.-H.; Cui, Y.; Wang, Z.-J.; Pan, Q.-Y.; Liu, K.; Sun, B.; Zhou, H.; Li, M.-J.; Xu, Q.; et al. Upgrade of Macromolecular Crystallography Beamline BL17U1 at SSRF. *Nucl. Sci. Tech.* **2018**, *29*, 68, doi:10.1007/s41365-018-0398-9.
72. McCoy, A.J.; Grosse-Kunstleve, R.W.; Adams, P.D.; Winn, M.D.; Storoni, L.C.; Read, R.J. Phaser Crystallographic Software. *J. Appl. Crystallogr.* **2007**, *40*, 658–674, doi:10.1107/S0021889807021206.
73. Emsley, P.; Cowtan, K. Coot: Model-Building Tools for Molecular Graphics. *Acta Crystallogr. D Biol. Crystallogr.* **2004**, *60*, 2126–2132, doi:10.1107/S0907444904019158.
74. Adams, P.D.; Grosse-Kunstleve, R.W.; Hung, L.W.; Ioerger, T.R.; McCoy, A.J.; Moriarty, N.W.; Read, R.J.; Sacchettini, J.C.; Sauter, N.K.; Terwilliger, T.C. PHENIX: Building New Software for Automated Crystallographic Structure Determination. *Acta Crystallogr. D Biol. Crystallogr.* **2002**, *58*, 1948–1954, doi:10.1107/s0907444902016657.